Nano-structural features of barite crystals observed by electron microscopy and atom probe tomography

Authors

Juliane Weber[1]*, Juri Barthel[2], Felix Brandt[1], Martina Klinkenberg[1], Uwe Breuer[3], Maximilian Kruth[2], Dirk Bosbach[1]

[1]Institute of Energy and Climate Research (IEK-6) – Nuclear Waste Management and Reactor Safety, Forschungszentrum Jülich GmbH, 52425 Jülich, Germany

[2]Central Facility for Electron Microscopy (GFE), RWTH Aachen University, 52074 Aachen / Ernst Ruska-Centre for Microscopy and Spectroscopy with Electrons (ER-C), Forschungszentrum Jülich, 52425 Jülich, Germany

[3]Central Institute for Engineering, Electronics and Analytics (ZEA-3), Forschungszentrum Jülich GmbH, 52425 Jülich, Germany

Highlights (3-5 bullet points, maximum 125 characters including spaces each)

- First time characterization of barite with a complementary approach of electron microscopy and atom probe tomography
- Identification of microstructural reasons for the high reactivity of a special barite type (SL barite)
- Microstructure of SL barite consists of micrometer sized macropores and nano-scale pores
- High resolution chemical analysis indicates that the nano-scale pores contain water and sodium chloride

Abstract

For the first time a barite sample was investigated by applying electron microscopy and atom probe tomography in a complementary approach to characterize its inner microstructure. Pores covering the size range from a few nanometers to a few micrometers were identified inside particles of a commercially available high purity barite. The barite matrix appeared to be a single crystal. A particular feature of the observed porous structure is a system of layers containing a high number of homogeneously distributed nano-scale pores, alternating with layers containing a limited number of

larger pores. High-resolution chemical analyses indicate that the pores contain a solution of water and sodium chloride. The filling of these nano-scale inclusions were interpreted as residua of the initial supersaturated solution used for particle growth by precipitation. These findings explain the high reactivity observed in previous Ra uptake studies on the same type of barite and provide further implications for the interpretation of these results. Our results offer a new analytical approach and necessary reference data for future investigations on changes of the internal barite structure during these Ra uptake experiments.

Key words

Barite, Electron Microscopy, Atom Probe Tomography, microstructure

1. Introduction

Barite ($BaSO_4$) is the most common barium mineral formed at low temperatures (Deer et al., 2013; Rösler, 1987) and is characterized by a very low solubility (Hanor, 2000). In nature, barite occurs as a gangue mineral in hydrothermal veins or as cavity filling in limestones, sandstones, shales and clays. It is also present as surface deposits and as a residual of limestone weathering (Deer et al., 2013). Solid solution formation between $BaSO_4$ and other sulfates such as $SrSO_4$, $PbSO_4$, and $RaSO_4$ or by exchange of the anion, e.g. by CrO_4. has been investigated repeatedly over decades due to the potential environmental implications (Becker et al. 2006; Bosbach et al., 2010; Boström et al. 1967; Burkhard, 1973; Ceccarello et al. 2004,; Grahmann, 1920; Prieto et al., 1997; Prieto et al., 1993; Putnis et al., 1992; Sabine & Young, 1954; Takano & Watanuki, 1974).

The formation of the $(Ba,Ra)SO_4$ solid solution raises problems in a number of industrial processes, leading to contamination by naturally occurring radioactive material (NORM) (Grundl & Cape, 2006; Minster et al., 2004; Zielinski & Otton, 1999). On a global scale, NORM created by the $(Ba,Ra)SO_4$ solid solution dominates the radioactivity originating from the production of gas and oil and geothermal energy (Eggeling et al., 2013; Zielinski et al., 2001). Recently, barite scale formation during hydraulic fracturing was observed. Here, Ra contamination of the barite scale plays an important role in a minority of wells (Zhang et al., 2014, 2015; Renock et al., 2016). Beginning with the early works of Doerner and Hoskins (1925); Gordon & Rowley, (1957) and Marques (1934) up to

recent publications (Curti et al., 2010; Rosenberg et al., 2011; Zhang et al., 2014), the fate of Ra in contact or during co-precipitation with barite has been studied. A very specific case in this context is the replacement of a pre-existing barite by a $(Ba,Ra)SO_4$ solid solution, which has been recently investigated with regard to safety assessments for the direct deep geological disposal of spent nuclear fuel (Bosbach et al., 2010; Brandt et al., 2015; Curti et al., 2010; Klinkenberg et al., 2014). In both cases, the barium concentration is typically orders of magnitude higher than the Ra concentration. Therefore the precipitation of a mixed $(Ba,Ra)SO_4$ phase lowers the concentration of Ra compared to the case of pure $RaSO_4$ precipitation (Jaremalm et al., 2013; Vinograd et al., 2013).

Starting from a pure barite in contact with a Ra-bearing solution, the formation of homogeneous $(Ba,Ra)SO_4$ particles in batch experiments has been demonstrated at the resolution of time-of-flight secondary ion mass spectrometry (Brandt et al., 2015; Klinkenberg et al., 2014). Scanning electron microscopy (SEM) observations on two different barites have shown that this reaction displays the typical features of a replacement reaction, i.e. the morphology and grain size of the barite after Ra uptake remain similar (Klinkenberg et al., 2014). The kinetics of the Ra uptake of the same barite types as in Klinkenberg et al. (2014) were described in Brandt et al. (2015). The latter study indicated a higher reactivity of the coarser grained barite compared to the other, fine grained barite with a much higher specific surface area. Brandt et al. (2015) concluded that normalizing the rate of Ra uptake to the surface area as determined by the BET method (Brunauer et al., 1938) may not be appropriate for describing the dissolution-reprecipitation processes controlling the replacement of pure barite by $(Ba,Ra)SO_4$.

A complete re-arrangement of the internal structure of the original barite particles can be expected for this process (Ruiz-Agudo et al., 2014). In order to characterize and understand the internal features of the barites which may contribute to their reactivity during the replacement, the application of true-nanometer scale resolution techniques is required. Recently, the combination of transmission electron microscopy (TEM) and atom probe tomography (APT) have provided new data in the case of glass dissolution. Based on these results the consideration of glass dissolution as a dissolution-reprecipitation process was further strengthened (Geisler et al., 2015; Gin et al., 2013; Hellmann et al., 2015; Putnis, 2015).

Here, we have applied a range of electron microscopy techniques for the detailed investigation of the internal microstructure of the same type of barite, which was the coarse barite with high reactivity used for Ra uptake experiments in several earlier studies (Bosbach et al., 2010; Brandt et al., 2015; Curti et al., 2010; Klinkenberg et al., 2014). Barite is known to contain different degrees of impurities of anions and cations, which are often associated with fluid inclusions (Bao, 2006). We therefore have accompanied the electron microscopy characterization in a complementary approach with APT. The elemental composition information obtained by APT is to a certain degree superior compared to energy-dispersive X-ray spectroscopy (EDX) as it provides near to atomic chemical and spatial resolution in particular for elements with low atomic numbers.

2. Materials and Methods

2.1. Barite sample

The material studied in this work is a commercially available high-purity barite (Blanc Fixe XR-10, Sachtleben GmbH, Germany) synthesized by precipitation according to the manufacturer information (Sachtleben, 2015). A high purity of the material with > 99.9 % $BaSO_4$ content was verified by X-ray diffraction (XRD) and SEM-EDX. Subsequently, the barite particles were separated to obtain a grain size fraction of ~6 – 45 µm. Finally, the material was equilibrated as described for the Ra-free reference sample named "reference SL" in Klinkenberg et al. (2014). First, the barite powder was equilibrated in pure water for 6 weeks. Afterwards, the grain size fractionation was performed by sedimentation using Atterberg cylinders. In a second equilibration step the barite powders were equilibrated in a suspension with 10 mL of 0.2 n NaCl solution for 4 weeks. The barite of the present study will be referred to as SL barite throughout this study and represents the starting condition of the barite before the uptake of Ra.

2.1. Sample preparation

Barite samples were extracted from an isopropanol suspension, dried on a Si-wafer, and coated with a carbon layer of approximately 20 nm thickness using a Quorum Q150T E sputter coater (Quorum

Technologies Ltd., U.K.). For the structural characterizations TEM lamellae and needle-shaped APT specimen, so-called APT tips, were cut from the barite particles using a focused $^{69}Ga^{+}$ ion beam (FIB) instrument. TEM lamellae were prepared in two different orientations: (i) cross-sections perpendicular and (ii) plane view lamellae parallel to the particles surface. A thickness < 100 nm is required of the TEM lamellae in order to achieve electron transparency (Williams & Carter, 2009). Due to the high sensitivity of the barite towards the Ga^{+} ion beam, the milling conditions had to be adapted to obtain lamellae fulfilling the thickness requirements of TEM. These adapted milling conditions applied with each working step are summarized in Table 1. The APT analysis requires a sample in the shape of a very sharp needle with an apex diameter of 50 – 100 nm in order to enable field evaporation of atoms (Kelly & Larson, 2012). Different types of FIB instruments were used depending on the availability and on the suitability of the equipment for the individual desired sample preparation procedure. The specification of the applied FIB instruments is given in the descriptions of the preparation procedures.

Preparation of cross-section TEM lamellae

Cross-section lamellae were extracted from the barite particles perpendicular to a selected surface. In general, the cross-section sample preparation was performed according to well-established procedures (Gianuzzi & Stevie, 1999; Mayer et al., 2007) using a Zeiss NVision 40 Cross Beam workstation (Carl Zeiss AG, Germany). The instrument is equipped with a GEMINI high-resolution field emission electron gun and a high performance S II NT zeta FIB column, thus providing a combination of ion milling and sample characterization by SEM. Additionally, the instrument comprises an INCA EDX detector (Oxford Instruments, U.K.). Regions with one cross-section axis parallel to the longest particle axis were chosen in order to obtain cross-sections of maximum area. A protective layer of around 3 µm thickness of either carbon (C) or platinum (Pt) was deposited on the region of interest. Afterwards, a ~ 1.5 µm thick slice was cut out of the bulk material and attached to the middle post of an Omniprobe TEM-grid (Oxford Instruments. U.K.). The lamella was thinned to < 100 nm in three steps, where the inclination angle and the beam current were reduced with each step. Subsequently, the lamellae were finalized with a low kV polishing to reduce amorphization and Ga implantation at the sample surface. Finally, the thinned cross-section lamellae had a size of 15 ± 5 µm x 7 ± 5 µm and were electron transparent in most areas.

Preparation of plan-view TEM lamellae

Plan-view lamellae are thin slices cut out parallel to the crystal surface. The plan-view preparation was generally performed according to Stevie et al. (1998) with an FEI Helios Nanolab 400S (FEI Company, The Netherlands) dual beam instrument equipped with the necessary flip-stage for this preparation procedure. The milling conditions adapted for the barite particles are given in Table 1. In contrast to the cross-section preparation described in the previous section, where a preliminary lamella was cut out, a thick wedge is removed from the particle in the plan-view preparation procedure. First, a protective Pt layer of around 1 µm thickness was deposited on a selected rectangular surface area of the particle (Figure 1 a). The selected area has a size of around 4 µm x 20 µm, defining the target size of the final TEM lamella. A wedge of material was cut out by milling rectangular regions on three sides of the protected area (Figure 1 b). Then, the wedge was connected with Pt to an in situ Omniprobe nano-manipulator (Oxford Instruments, U.K.). The stage with a Cu Omniprobe TEM grid was flipped by 90° and the sample wedge was attached to the grid with Pt (Figure 1 c+d). In order to protect the target volume from beam damage and Ga implantation during the final milling steps towards a thin lamella, two Pt layers were deposited on a selected area of the wedge (Figure 1 d+e). Subsequently, the upper and lower parts of the wedge were milled in several steps shaping the sample into a lamella of ~20 nm thickness (Figure 1 f - h). Finally, amorphization and Ga implantation were reduced on the milled sides by the application of a low-kV polishing step.

169 Table 1 Milling conditions for the preparation of cross-section and plan-view TEM
170 lamellae of barite particles.
171

Working step	Milling conditions	Sample tilt
Cross-section TEM lamellae		
Cut out of the lamella < 1.5 µm		
Trapezia	30 kV, 300 pA	
Rectangle	30 kV, 300 pA	1.0°
Thinning of the lamella < 100 nm		
Step 1	30 kV, 80 pA	1.0°
Step 2	30 kV, 40 pA	0.8°
Step 3	30 kV, 60 pA	0.6°
Low kV polishing	2 kV, 25 pA	2.0°
Plan-view TEM lamellae		
Cut out of the wedge	30kV, 6.5 nA	
Thinning of the lamella < 100 nm		
Step 1	30 kV, 460 pA	1.5°
Step 2	30 kV, 280 pA	1.2°
Step 3	30 kV, 93 pA	0.8
Low kV polishing	5 kV, 47 pA	2.0

172

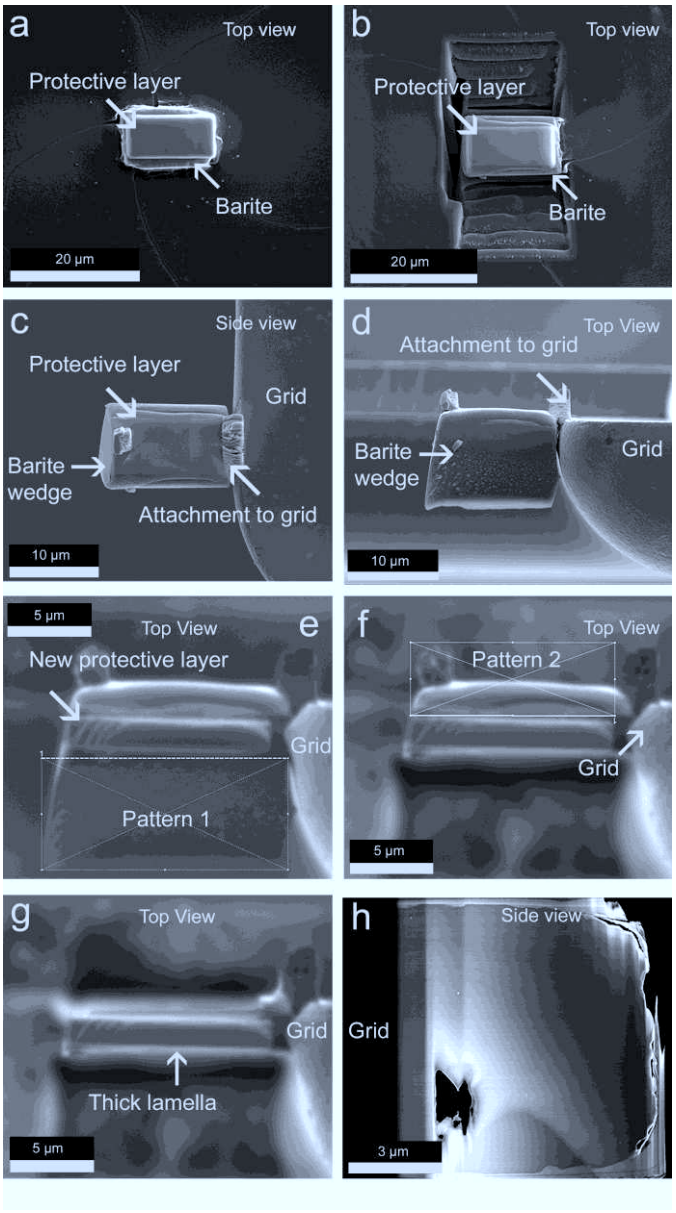

Figure 1 Plan view lamellae preparation. a) Top view of the barite particle with a protective layer on top. b) Top view of the barite particle with cut-out trenches. c) Side view of the wedge attached to the grid. d) Top view of the wedge attached to the grid. e) Top view showing the new protective layer and the first milling pattern. f) Top view of the second milling pattern. g) Top View of the lamella shaped sample before the final ion beam thinning steps. h) Side view of the thin lamella.

Preparation of APT tips

The tips for APT were prepared with a FEI Helios 600 dual beam instrument based on the procedures of Miller et al. (2005 & 2007), Miller & Russel (2007) and Thompson et al. (2007). Similar to the previously described TEM lamellae preparation procedure, the barite particles were first fixed to the Si substrate with Pt. Then, a protective layer of Pt with ~200 nm thickness was deposited (5 kV, 120 pA) on a rectangular region of interest of 2 µm x 20 µm size. A wedge of barite was cut out below the protective layer on three sides (30 kV, 0.79 nA). Before removing the final connection, this wedge was

attached to an in situ nano-manipulator (Omniprobe, Oxford Instruments, U.K.) using Pt as shown in Figure 2a. The barite wedge was then moved to the Si posts of a 22-array coupon (Cameca Scientific Instruments, USA). After attaching the wedge to one of the posts with Pt, 1 - 2 µm thick segments were cut off as displayed in Figure 2b. Subsequently, each tip was sharpened by using an annular milling pattern by stepwise reduction of the inner and outer diameter and reducing the beam currents (30 kV, 0.23 nA to 30 kV, 20 pA). A variety of beam currents were applied in order to shape the sample segments into a sharp needle as the segments exhibited different reactions to the ion beam milling. This behaviour indicates inhomogeneous properties of the barite particles. The obtained tips had apex diameters of 50 – 80 nm (Figure 2c).

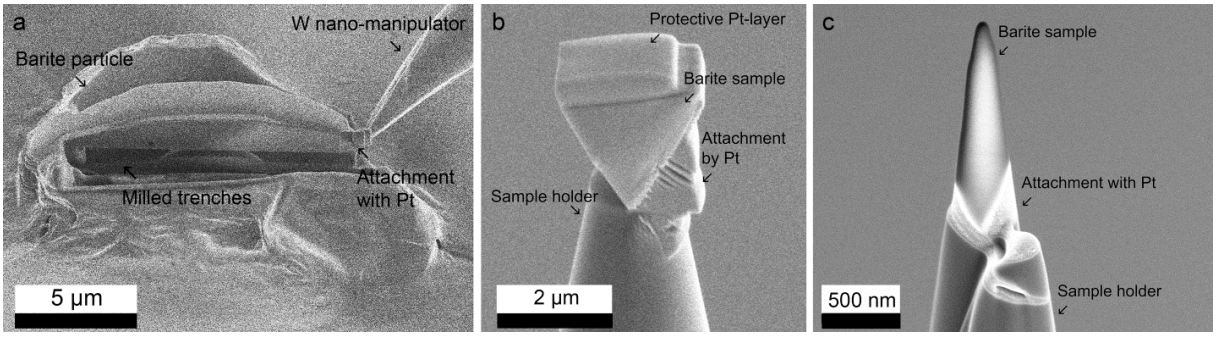

Figure 2 Stages of the APT tip preparation. a) Milling of trenches and attachment of nano-manipulator to the sample b) sample chunk attached to the sample holder c) sample ready for measurement in APT, final radius is ~ 70 nm.

2.2. Transmission electron microscopy

Selected area electron diffraction (SAED) images and scanning transmission electron microscopy (STEM) images were recorded with an FEI Tecnai G^2 electron microscope operated at an accelerating voltage of 200 kV. The STEM images were acquired with a high-angle annular dark-field (HAADF) detector setup. For thin samples the HAADF image intensity is proportional to the atomic numbers accumulated in the sample volume traversed by the electron beam, thus providing a certain degree of information about local variations of chemical composition, density, and sample thickness (Williams & Carter, 2009).

The elemental distribution was mapped by EDX with an FEI Titan G2 80 – 200 electron microscope equipped with an EDX system in the ChemiSTEM^{TM} design (FEI Company, The Netherlands) which

212 was operated at 80 kV accelerating voltage with a 500 pA probe current. The ChemiSTEM^{TM} design
213 comprises four large-area, windowless SDD detectors which are oriented annular in the Super-X^{TM}
214 geometry around the sample area. A particular challenge of the TEM investigations is the relatively
215 low stability of barite under high-energy electron irradiation of the electron beam, e.g. the thinned
216 barite crystal disintegrated within seconds when applying the high current densities required for high-
217 resolution imaging. A longer acquisition of EDX maps for more than several minutes was possible by
218 adjusting the STEM setup to reduced probe currents of less than 500 pA and applying 80 keV primary
219 electron energy.
220
221 **2.3. Atom probe tomography**
222 Atom probe tomography is a technique capable of providing a 3-dimensional reconstruction of the
223 elemental composition in a tip-shaped sample at near-to-atomic resolution based on mass spectrometry
224 data. In a laser APT experiment different ionic species are extracted from the sample surface by
225 electric field evaporation triggered by a laser pulse. These ions are registered according to their time-
226 of-flight. The time-of-flight data are transformed into a mass-to-charge ratio (m/n), which is denoted
227 in relative atomic mass and elementary charge units consistently throughout this study. This approach
228 leads to a certain degree of ambiguity for the identification of chemical species as different ions or
229 ionic molecules may have very close or even the same mass-to-charge ratio. In practice, the natural
230 isotopic ratios of the elements can often help to overcome these ambiguities, thus providing a high
231 yield of unique chemical information. Based on prior knowledge about the sample geometry and the
232 resulting electric field, the data of the position-sensitive detector can be reconstructed to the original
233 3D atom position in the sample (Kelly & Larson, 2012).
234 Our APT measurements were performed with a LEAP 4000X HR instrument using a laser wavelength
235 of 355 nm (Kelly & Larson, 2012). The mass resolving power of this instrument is > 1000 FWHM at
236 m/n = 27 for a 100 nm wide field-of-view. During the measurement the specimen was cooled to a
237 temperature of 50 K and a voltage of 2 - 7 kV was applied to generate the evaporation field. Several
238 instrument parameters had to be modified individually in each measurement in order to maximize the

ion detection yield. The laser energy was tuned between 40 and 55 pJ per pulse at 160 to 250 kHz pulse rates, and the base voltage was adjusted to maintain a detection level of 0.005 atoms per pulse.

The atom probe data was analysed with the Cameca IVAS Software Version 3.6.8. A tomographic reconstruction of the sample volume from the time-of-flight data requires either knowledge of the shank angle or of the threshold for the initiation of electric field evaporation (Kelly & Larson, 2012). In the present study we had to estimate the shank angle from preceding SEM observations because the electric field required to start field evaporation from a barite surface is unknown.

The failure rate of measurements due to sample breakage was around 60 %, probably occurring due to the presence of macropores in the APT tips. However, reasonably large datasets were aquired for several samples consisting of > 30 Mio. detected ions even though barite is neither electrically conductive nor a very good thermal conductor (Horai, 1976). The datasets presented in this paper contain between 90 and 93 % single hit registrations, 6 – 9 % multiple hits, and about 1 % partial hits. Only single hit data has been used for tomographic reconstruction.

3. Results & Discussion

3.1. SEM observations

Nine cross-sections were obtained from representative barite particles which exhibited a blocky or nearly euhedral morphology as displayed in Figure 3. The most prominent feature of the SEM images is a crystallographic oriented system of contrast variations, which indicates the presence of a layered structure. For the nearly euhedral particles, the layers are arranged systematically, parallel to the outer surfaces, see Figure 3a. Possible reasons for the observed contrast variations can be chemical variations, crystal defects leading to orientation variations, and density variations, such as nano-scale porosity which has been described e.g. for feldspars (Ruiz-Agudo et al., 2014). EDX mapping of cross-sections indicated no compositional zoning within the error of the measurement. This is in good agreement with the available literature.

Previous studies on natural barite samples (Frondel, 1935; Lendeking & Wheeler, 1891; Parr & Chang, 1935) showed both the layered structure as well as the homogeneous barium sulphate composition within the error of the measurement. Therefore, the EDX mappings on the SL barite

cross-sections and the studies of Frondel (1935), Lendeking & Wheeler (1891) and Parr & Chang (1935) are consistent.

In addition to the layered structure, macropores of irregular shape and a few micrometer in diameter were present in most of the FIB cross-sections. In a few cases we observed macropores of elongated shape, located along the track of the layered structure, e.g. in Figure 3b. Because the macropores were opened during FIB milling under high-vacuum it remains unclear whether they initially contained gaseous or fluid inclusions. No precipitates were detected in the opened macropores by EDX.

Barites from natural deposits have been reported to contain micrometre-scale fluid inclusions (Bodnar, 2014; Böhlke & Irwin, 1992; Rajabzadeh, 2007; Wilkinson, 2001), which could potentially correspond to the macropores observed in the synthetic barite here by SEM. A correlation to natural barites is reasonable, as both the synthetic SL barite and most of the natural barites are formed by precipitation from an aqueous solution under similar conditions. For natural barites the precipitation is typically induced by mixing of fluids resulting from the alteration of silicate, carbonate, and sulfate minerals in sedimentary, metamorphic, and igneous rocks (Hanor, 2000). Often, fluid inclusions of micrometre size in natural barites are lens-shaped and contain no daughter minerals (Bodnar, 2014; Böhlke & Irwin, 1992; Rajabzadeh, 2007; Wilkinson, 2001). Furthermore, Rajabzadeh (2007) reported fluid inclusions matching the cleavage planes of the barite crystal, which could correspond to the elongated pores observed here (Figure 3b). Accordingly, there are several indications that the macropores observed in the cross-sections may indeed have contained a fluid before they were opened during the FIB-milling.

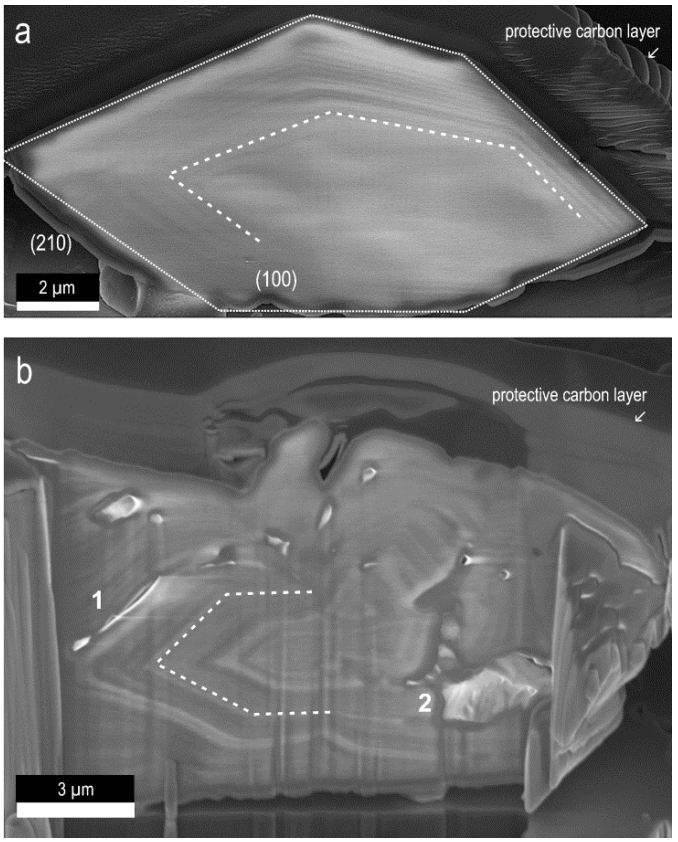

Figure 3 Cross-sections of the SL barite particles. The particles exhibited (a) nearly euhedral shapes and (b) blocky shapes. The outer crystal faces in (a) are marked by a solid line. The layered structure is visible in both cross-sections as indicated by a dashed line. The particle in (b) contains a diversity of macropores, such as (1) elongated pores tracing the layered structure and (2) larger, randomly oriented pores.

3.2. Selected Area Electron Diffraction

In order to determine if the layered structure observed in SEM could be due to variations of the crystal orientation, electron diffraction patterns were acquired from a thin TEM lamella. The electron diffraction pattern recorded from an area containing several layers (Figure 4a), corresponds to $BaSO_4$ in [001] zone axis orientation (Figure 4b). No additional reflexes were observed in this pattern, which indicates a single crystalline, coherent structure without twins, grain boundaries, or other large scale defects.

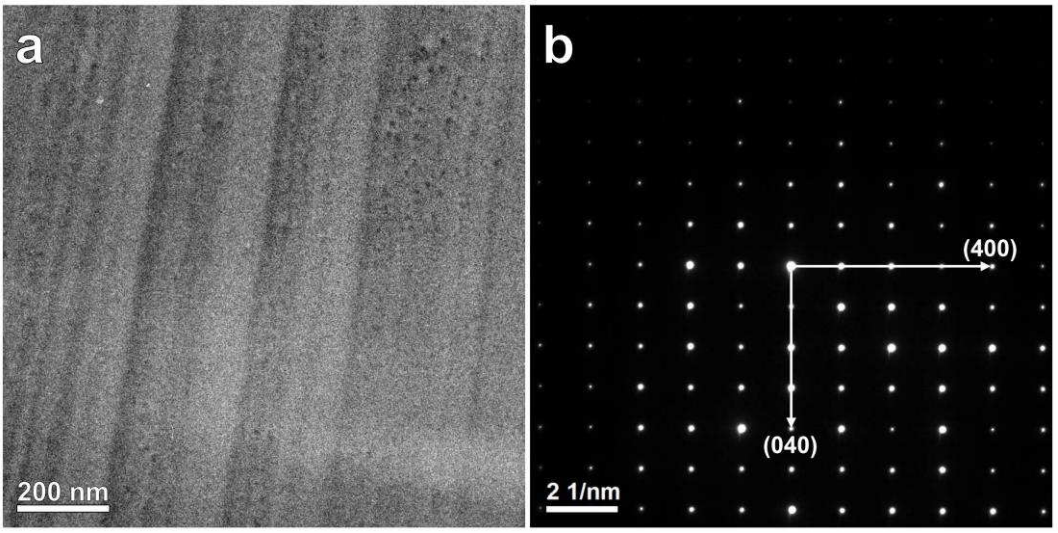

Figure 4 Electron Diffraction analysis. (a) HAADF STEM image and (b) electron diffraction pattern recorded from a large area of a thin barite lamella containing several layers of dark and bright HAADF signal.

Small variations of the crystal axis between the layers could still be hidden in the average, large-area diffraction pattern of Figure 4b. Therefore, additional diffraction patterns were obtained from small selected areas of the crystal, ideally only containing the diffraction signal from one type of layer. Figure 5 displays a sequence of selected area electron diffraction (SAED) images, where a sufficiently small area selecting aperture was moved across the layered structure. The positions, where the diffraction patterns were recorded are marked by circles in Figure 5a. The diffraction patterns registered at the respective positions are displayed in Figure 5b1-b8, showing again the diffraction pattern of a single crystalline $BaSO_4$ in [001] orientation. No significant variation of beam excitations and beam positions was detected over the sequence of eight patterns. In conclusion, the contrast variations visible in the TEM images cannot be attributed to variations of the crystal orientation.

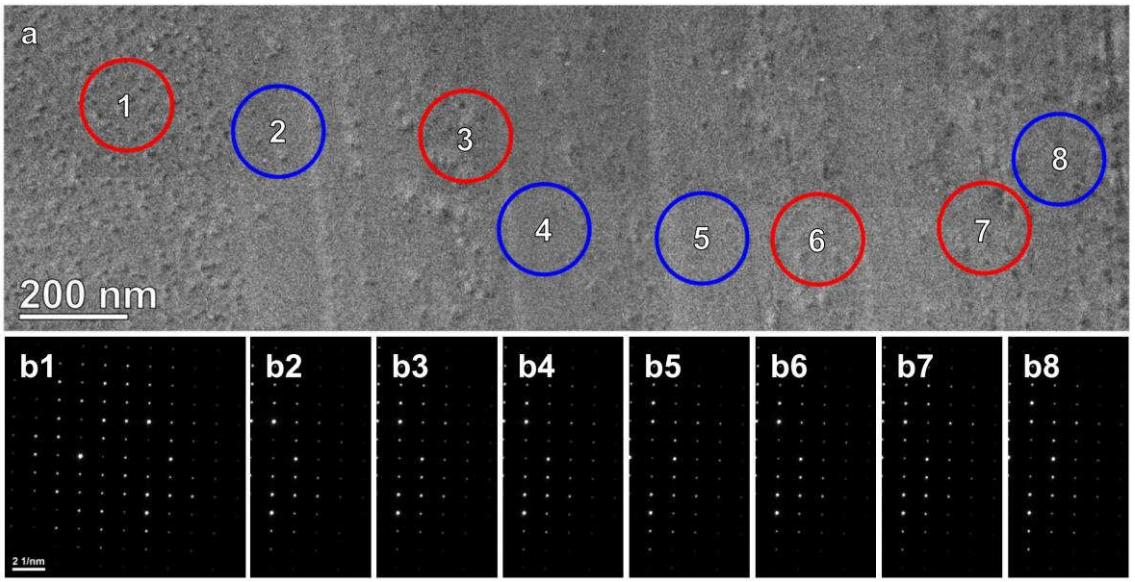

Figure 5 Selected Area Electron Diffraction experiment. (a) HAADF STEM image of the layered structure with circular regions marking the positions of a sequence of SAED experiments. Red circles mark areas of layers containing a high density of dark spots, while blue circles mark homogeneous brighter layers. (b1) - (b8) Electron diffraction patterns recorded from the respective areas marked in (a).

3.3. Scanning Transmission Electron Microscopy

Figure 6 displays an HAADF STEM image of a complete cross-section lamella prepared from a blocky barite particle oriented with the [001] crystal zone axis along the viewing direction. The cross-section contains a macropore in the centre, and the aforementioned layered structure again appears as crystallographically well oriented layers of alternating higher and lower intensity. The strongest contrast variations in Figure 6 appear with a density of about 2 - 3 dark zones per micrometer with irregular thickness and distance.

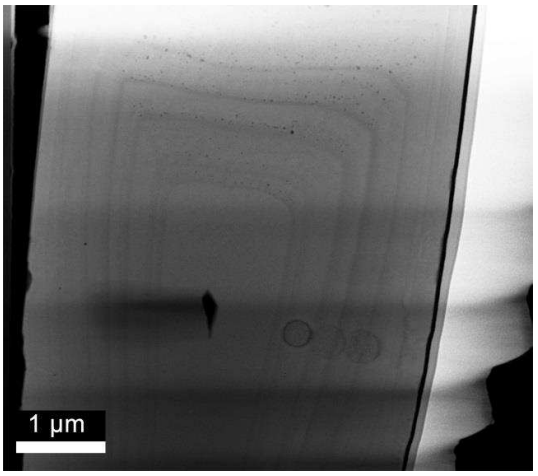

Figure 6 HAADF STEM image of the SL barite. It clearly shows a layered structure of alternating high and low intensity. The black region in the center is a macropore, while the circular features to the right of the pore are due to sample damage induced by the electron beam. Horizontal contrast variations are due to global thickness variations caused by inhomogeneous ion beam thinning.

However, simultaneously recorded elemental maps of the same area do not show respective signal variations as observed in the HAADF signal. This observation is in agreement with the preceding SEM observations. In the HAADF images of all the investigated TEM lamellae the layered structure was clearly visible across the full area independent of the sample thickness. The layered structure was observed similarly in both, plan-view and cross-section lamellae. This confirms its 3-dimensional nature.

HAADF STEM images taken at higher magnification as displayed in Figure 7 indicate a structural difference between the alternating layers on the nanometre scale. Almost circular regions of low HAADF intensity are apparent in different size and number, which can be interpreted as pores or inclusions of low-Z material in the barite matrix. While the bright zones contain larger pores with diameters around 10 – 70 nm in a lower density, the dark zones comprise a very high density of smaller pores of only a few nanometres size.

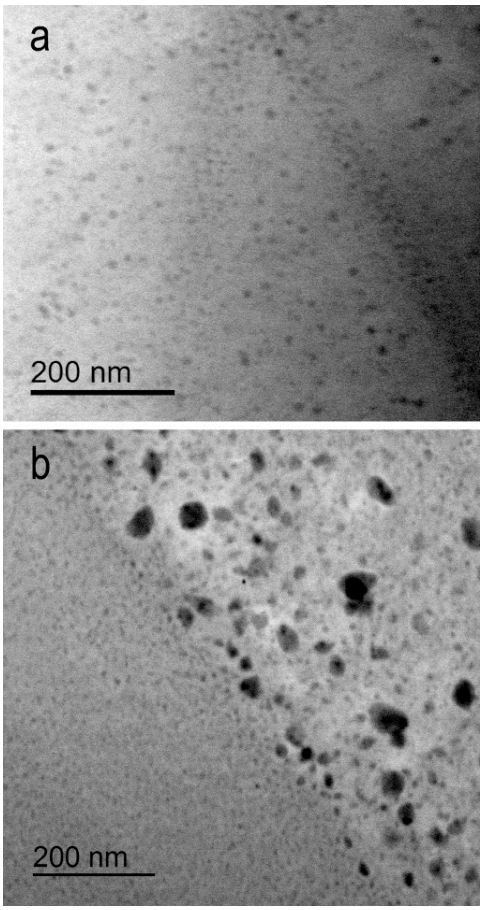

Figure 7 HAADF STEM images of the SL barite. a) Upside down V-shaped layered structure in a barite cross-section lamella. The intensity variation from the left to the right side of the image is due to thickness variations in the lamella. b) Inter-face between a bright zone (right) and a dark zone (left) of the layered structure in a barite plan-view lamella. In both images, the bright layer contains larger pores in a lower density, while the dark layer shows a very high density of smaller pores.

Because neither a secondary phase nor variations of composition and orientation were detected by EDX and electron diffraction, the lower HAADF intensity indicates the presence of nano-scale porosity. These pores are distributed across the whole crystal volume. It can be concluded that the crystallographically oriented layers of dark and bright intensity apparent in SEM and STEM images are due to a variation of the pores' density and size. Based on the electron microscopy data alone it is not possible to determine whether these pores are empty or contain material of low scattering power.

In principal, there are two different explanations for our results that are already described in literature. Nano-scale porosity in barite crystals has already been observed by time-resolved TEM investigations performed during its crystal growth (Judat & Kind, 2004; Ruiz-Agudo et al., 2015). It has been concluded there, that the small pores are residuals of a growth mechanism proceeding via a combination of molecular growth and oriented self-assembly of nano-crystals from a supersaturated

aqueous solution. A final internal re-crystallization process leaves pores of a few nanometres size, which are possibly filled with a residual liquid. In the literature, the size and density of the pores was reported to depend on the initial level of supersaturation. The barite particles of our study have a size of ~20 µm whereas Ruiz-Augo et al. (2015) reported nano-porosity in µm-size crystals.

Despite these non-classical nucleation path theories, the defects could also stem from a synthesis with a high saturation index which is most likely as it reduces synthesis time and therefore costs. Sponanteous formation of unfilled cores with nm to µm size during crystal growth has been shown e.g. in potassium dihydrogen phosphate crystals (Zaitseva & Carman, 2001; De Yoreo et al., 2002).

Another possibility for the origin of pores inside barite crystals would be that sodium chloride interacts with the step edge during crystal growth and then is incorporated as a trace impurity. Sometimes it could also create a defect which leads to a defect formation such as unfilled cores. Becker et al. (2002) showed that the NaCl concentration has a strong effect on step velocities and morphologies. These findings were strengthened by Godinho and Stack (2015) who demonstrated that the overall crystal morphology and rate are also affected by the NaCl concentration.

3.4. Atom Probe Tomography

APT of the barite samples has been performed in order to answer the question whether the observed pores are empty or contain material benefitting from the superior chemical resolution of this technique compared to EDX. The measured mass-to-charge ratio spectra of the barite samples, e.g. as displayed in Figure 8 are dominated by a peak at m/n = 69, which corresponds to the two ionic species $^{138}Ba^{2+}$ and $^{69}Ga^{+}$. Because other Ba^{2+}-peaks were also detected with intensities reproducing the expected natural ratios of Ba isotopes, we fully assigned the dominant peak to $^{138}Ba^{2+}$. Thereby we omit a probably very small Ga^{+} signal which could originate from a Ga^{+} ion implantation during the FIB milling. The $^{138}Ba^{2+}$ peak at m/n = 69 constitutes 81 – 95 % of the total detected amount of Ba in a sample. Therefore, we have chosen this peak of the mass-to-charge ratio spectrum for the display of the 3D reconstructions in Figure 9. Clear signals of species containing sulphur and oxygen are present in the spectrum. Additional peaks are visible indicating the presence of H_2O, Na, and Cl in minor amounts.

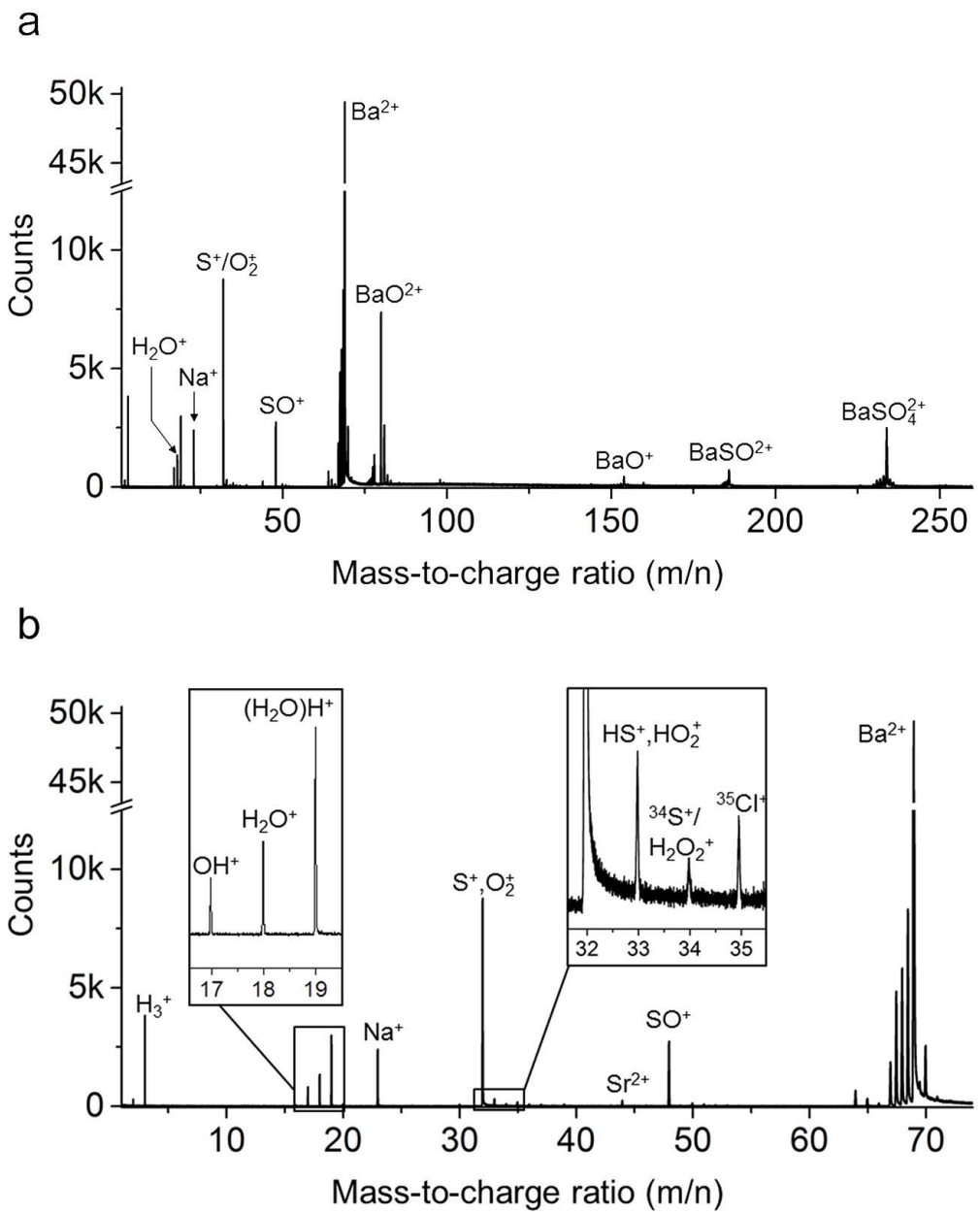

Figure 8 APT mass-to-charge ratio spectrum. a) Typical APT mass-to-charge ratio spectrum of the analyzed barite. The dominating peak is Ba^{2+} at m/n = 69. Other strong peaks are marked, such as those of H_2O^+ and Na^+ ions. b) Lower region of the mass-to-charge ratio spectrum. The left inset displays a magnification of the spectrum with variants of ionic water species. The right inset displays the region from m/n = 32 to 35, containing signals of sulfur and chlorine ions.

A list of all the observed peaks and their assignments to specific ions for both measurements presented here are listed in Table 2. Due to the application of different pulse rates, the mass range is different in both measurements. Many Ba-containing molecules such as BaO^+, $BaSO^{2+}$, and $BaSO_4^+$ are present in the list. The formation of molecules during the measurement of complex materials has been observed

earlier in other materials, e.g. semiconductor or dielectrics. For example Gordon et al. (2012) reported the formation of various molecules in APT characterization of different apatites.

Table 2 Peaks observed in the APT measurements of the SL barite and identified ionic species.

Barite 1		Barite 1		Barite 2		Barite 2	
m/n	Identified Species	m/n	Identified Species	m/n	Identified Species	m/n	Identified Species
3	H_3^+	82	SO_3^+	2	H_2^+	69	Ba^{2+}
17	OH^+	154	BaO^+	3	H_3^+	69.5	HBa^{2+}
18	H_2O^+	185	$BaSO^+$	17	OH^+	70	H_2Ba^{2+}
19	$(H_2O)H^+$	185.5	$BaSO^+$	18	H_2O^+	76	BaO^{2+}
23	Na^+	186	$BaSO^+$	19	$(H_2O)H^+$	76.5	BaO^{2+}
32	S^+/O_2^+	-	-	23	Na^+	77	BaO^{2+}
33	$HS^{+/}HO_2^+$	-	-	32	S^+/O_2^+	77.5	BaO^{2+}
35	Cl^+	-	-	33	$HS^{+/}HO_2^+$	78	BaO^{2+}
43	Sr^{2+}	-	-	34	$S^{+/}H_2O_2^+$	80	SO_3^+
43.5	Sr^{2+}	-	-	35	Cl^+	81	SO_3^+/HSO_3^+
44	Sr^{2+}	-	-	36	HCl^+	82	SO_3^+
48	SO^+	-	-	37	Cl^+	98	$H_2SO_4^+$
64	SO^{2+}	-	-	38	HCl^+	144	$S_2O_5^+$
65	Ba^{2+}	-	-	39	NaO^{2+}	151	BaO^+
66	Ba^{2+}	-	-	43	Sr^{2+}	152	BaO^+
67	Ba^{2+}	-	-	44	Sr^{2+}	153	BaO^+
67.5	Ba^{2+}	-	-	48	SO^+	154	BaO^+
68	Ba^{2+}	-	-	49	H_2SO^+	185	$BaSO^{2+}$
69	Ba^{2+}	-	-	50	H_2SO^+	185.5	$BaSO^{2+}$
69.5	HBa^{2+}	-	-	51	H_2SO^+	186	$BaSO^{2+}$
70	H_2Ba^{2+}	-	-	52	H_2SO^+	187	$BaSO^{2+}$
76	BaO^{2+}	-	-	53	H_2SO^+	230	$BaSO_4^+$
76.5	BaO^{2+}	-	-	64	SO^{2+}	231	$BaSO_4^+$
77	BaO^{2+}	-	-	65	Ba^{2+}	232	$BaSO_4^+$
77.5	BaO^{2+}	-	-	66	Ba^{2+}	233	$BaSO_4^+$
78	BaO^{2+}	-	-	67	Ba^{2+}	234	$BaSO_4^+$
80	SO_3^+	-	-	67.5	Ba^{2+}	235	$BaSO_4^+$
81	SO_3^+/HSO_3^+	-	-	68	Ba^{2+}	236	$BaSO_4^+$

411 There are also some peaks present where the identification of the ionic species is ambiguous. In the
412 following some details of the mass-to-charge spectrum are explained concerning peaks which are
413 controversially discussed in the current literature, such as impurity peaks, peaks with unsolvable
414 interferences of ionic species, and peaks where the assignment remains questionable.
415 The lower region of the spectrum contains three strong and sharp peaks around m/n = 18, resembling
416 water species as highlighted by the left inset of Figure 8b. We interpret this as the signal of water
417 present in the barite sample. Our interpretation is based on the finding that the 3D distribution of these
418 signals is anti-correlated to the Ba signal (Figure 9). This indicates that the source of the oxygen in
419 these water species is not $BaSO_4$. We would exclude the alternative interpretation, which is that we see
420 a hydride formation of oxygen stemming from the $BaSO_4$. Such hydride formation is discussed in the
421 APT literature as an artifact occurring predominantly in the first stages of the measurement due to
422 outgassing of the stainless steel vacuum chamber (Gault et al., 2012; Miller & Forbes, 2014). Here, we
423 observed a very strong peak of hydrogen and water species during the whole measurement similar to
424 other studies where the specimen contains oxygen and hydrogen components (Gordon et al., 2012).
425 At m/n = 43 and 44 signals of Sr^{2+} with a peak height of about 0.5% compared to the strongest Ba^{2+}
426 peak are detected, indicating the presence of a low amount of Sr in some of the samples. Because
427 $BaSO_4$ and $SrSO_4$ form a solid solution and have a large affinity for each other, this impurity is often
428 observed in synthesized and natural barite crystals (Hanor, 2000).
429 A severe ambiguity exists for the two major components oxygen and sulfur, as the respective two
430 main ionic species S^+ and O_2^+ have the same mass-to-charge ratio m/n = 32. According to the ratios of
431 stable natural isotopes, a second sulfur peak is expected at m/n = 34 with 5 % intensity of the main
432 sulfur signal. Here we only observed a very small peak at m/n = 34, as shown in the right inset of
433 Figure 8b, indicating that the peak at m/n = 32 is predominantly due to O_2^+. One would then also
434 expect an O^+ peak at m/n = 16. This is, however, missing in all of our measurements, probably due to
435 the chosen instrumental parameters. Accordingly, the sulfur content of the sample is measured mainly
436 as a component of SO_x^{n+} and $BaSO_x^{n+}$ ionic molecules (Table 2). In general, the solution of
437 ambiguities by means of natural isotope ratios is complicated in this particular material due to the

presence of water, which adds additional interferences with the pure elemental signal because a diversity of hydrides may form.

The assignment of an ionic species to the peak at m/n = 70 is also ambiguous at first glance. Possible candidates with this mass-to-charge ratio are H_2Ba^{2+}, HGa^{+}, and Cl_2^{+}. In the case of chlorine, significant peaks would be expected at m/n = 72 and 74 due to the rather large natural fraction (25%) of the ^{37}Cl isotope. Because these two peaks do not occur here, we can exclude chlorine at m/n = 70. A strong HGa^{+} component in this peak would cause a noticeable signal in the 3D reconstruction, as Ga implantations should be located preferentially close to the surface of the tip sample. However, no location preference is present for the events detected with this mass-to-charge ratio. Accordingly, only H_2Ba^{+} remains as possible explanation. This assignment is further substantiated by the occurrence of a weak peak at m/n = 69.5, which would correspond to HBa^{2+}.

The reconstruction of the APT data for the analysed barite exhibits a previously undetected inhomogeneous distribution of Ba, H_2O, and Na, which is clearly visible in the projections displayed in Figure 9 a+c. Integrated concentration profiles calculated along the axis of a cylindrical sub-volume perpendicular to the layers are displayed in Figure 9c+d and show a prominent sequence of alternating layers of anti-correlated Ba and H_2O intensity. The signal of H_2O in these profiles is rather low, on the order of one per cent of the $BaSO_4$ signal. The partial correlation of the H_2O and Na signal indicates that the individual inclusions contain different degrees of Na. Cl could be associated with Na in fluid inclusions, although the Cl signal was too weak to produce a significant correlation. The very low yield of Cl species could be explained with a very low probability of Cl forming a positively charged ion. The layers of alternating chemical composition observed in the profiles have irregular sizes between 20 and 200 nm, similar to the layers of alternating HAADF intensity observed in the STEM images (Figure 6).

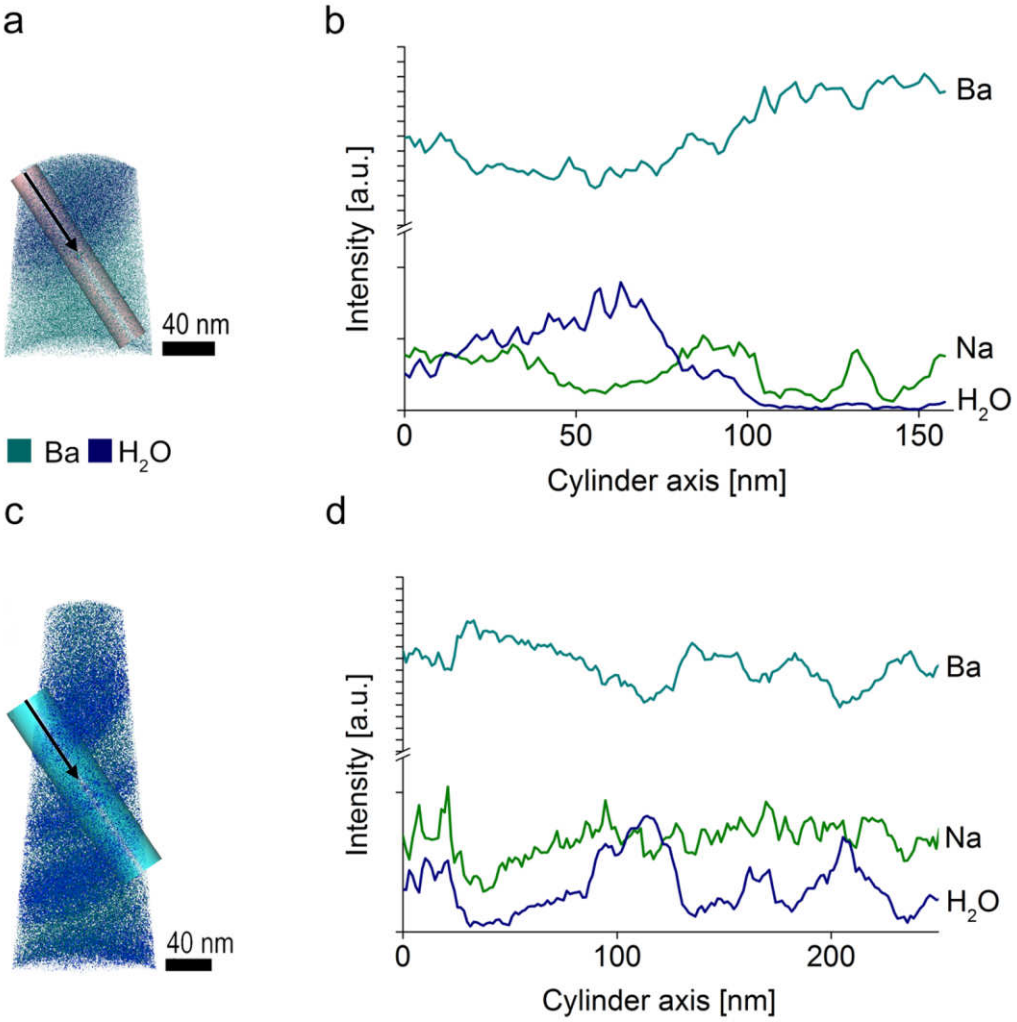

462

463 Figure 9 3D elemental composition reconstructions of two APT measurements of the SL barite.
464 A layered structure due to chemical variation is displayed: (a) and (c) reconstructions with selected Ba
465 and H_2O ions, (b) and (d) integrated intensity profiles calculated with a perpendicular orientation to
466 the layered structure along the axis of a cylinder sub-volume. The profiles indicate an anti-correlation
467 of the Ba and H_2O concentration across the layered structure. The Na signal is at least partially
468 correlated to the H_2O signal in (d).

469

470 Clusters of higher local H_2O concentration in the reconstructed 3D data, which resemble the
471 previously in HAADF images observed nano-scale pores, were smaller than 10 nm. Due to the
472 variations in the H_2O concentration it can be concluded that these nano-scale pores are inclusions of
473 water. In the HAADF images larger pores were also observed that are not present in the reconstructed
474 3D distribution of elements. A possible explanation for this is the fact that samples with larger pores
475 have a higher probability to break during the APT analysis. Nevertheless, the detection of a layered
476 structure in HAADF STEM images and in the APT reconstruction are consistent as H_2O, Na, and Cl
477 are low-Z elements which would produce a significantly lower HAADF signal compared to the the

478 $BaSO_4$ matrix. Consequently, regions of reduced HAADF intensity in the STEM images as visible in
479 Figure 6 and Figure 7 would correspond to the regions of higher H_2O and lower Ba concentration in
480 the projections and profiles of Figure 9. In combination, the findings of our STEM and ATP
481 measurements give evidence that the barite particles contain nano-scale pores including a fluid
482 solution of water and NaCl.
483
484 **4. Conclusions**
485 For the first time, a complementary analytical approach consisting of electron microscopy and atom
486 probe tomography was applied to unravel the details of the internal microstructure of a reference barite
487 sample. By the adaption of the beam currents used during the FIB sample preparation, a reliable
488 procedure was developed to prepare TEM lamellae and APT tips of barite. The APT measurements
489 were conducted successfully for the first time and reasonably large datasets consisting of more than 30
490 million detected ions were acquired. Within the barite, macropores with a size of a few micrometres as
491 well as of layers enriched in nano-scale inclusions filled with water and NaCl were identified. The
492 layers enriched in nano-scale inclusions are arranged predominantly parallel to the outer barite particle
493 surfaces. This indicates that the origin of the layered structure is related to the growth of the barite
494 particle by precipitation from a supersaturated solution. The precipitation most likely follows the
495 reaction:
496 $BaCl_2 + Na_2SO_4 \rightarrow BaSO_4 + 2\ NaCl$.
497 In this case, the identified composition of the nano-scale inclusions is consistent with the residuum of
498 the assumed mother liquid.
499 The SL barite reference sample characterized here was also used as the starting material in several
500 earlier studies regarding the uptake of Ra by pre-existing barite by Curti et al. (2010), Bosbach et al.
501 (2010), Klinkenberg et al. (2014) and Brandt et al. (2015). The results obtained by the new approach
502 have implications for the interpretation of data presented in the aforementioned studies. In the two
503 latter studies the observed reactivity of the SL barite was higher compared to the reactivity of another
504 barite type. The observed nano-scale inclusions are defects in the crystal structure which represent
505 possible pathways for the Ra to enter the barite solid. Moreover, the available surface for the assumed
506 dissolution and re-precipitation mechanism is increased significantly by taking into account the

additional interfaces between the barite particle and the nano-scale inclusions. This explains the higher reactivity of the SL barite.

The reviews of Stack (2015) and Anovitz (2015) cover the topic of the relationship between the reactivity of pores and their size. They propose a different reactivity of nano-scaled pores compared to bulk rocks. Applying this principle to interpret our results, the observed nano-scaled pores may present ideal nucleation sites for mixed phases of $(Ba,Ra)SO_4$ because their reactivity is different from the other present crystal surfaces.

Furthermore, the present study is a reference study for ongoing research. Further insights into the evolution of the Ra distribution and the microstructural changes in the barite with time can be expected by applying the complementary nano-analytical approach developed in the present work in future studies on Ra-containing barites.

ASSOCIATED CONTENT

Supporting Information

AUTHOR INFORMATION

Corresponding Author

*jul.weber@fz-juelich.de

Author Contributions

The manuscript was written through contributions of all authors. / All authors have given approval to the final version of the manuscript.

ACKNOWLEDGMENT

Prof. J. Mayer is acknowledged for fruitful discussions. We are grateful to A. Savenko for his support. The Swedish Nuclear Fuel and Waste Management Ageny (Svensk Kärnbränslehantering Aktiebolag) is acknowledged for partial financing of this study. J. Barthel and M. Kruth acknowledge funding within the core facilities initiative of the German Research Foundation (DFG) under the grant number MA 1280/40-1. The authors would like to thank Jordi Bruno and two anonymous reviewer for their reviews which helped to improve the manuscript.

535

536 REFERENCES

537 Bao, H. *Anal. Chem.* **2006**, 78(1), 304-309. DOI: 10.1021/ac051568z

538 Becker, U., Fernández-González, A., Prieto, M., Harrison, R., Putnis, A. *Phys. Chem. Min.* **2000**. 27,
539 291-300. DOI: 10.1007/s002690050258

540 Becker, U., Risthaus, P., Bosbach, D., Putnis, A., *Mol. Simulat.* **2002**. 28 (6-7), 607-632. DOI:
541 10.1080/08927020290030161

542 Bodnar, R.J., Lecumberri-Sanchez, P., Moncada, D., Steele-MacInnis, M. Fluid inclusions in
543 Hydrothermal Ore Deposits. In: Holland, H.D., Turekian, K.K. (eds.) Treatise on geochemistry, 2nd
544 edition, 13, **2014**, pp. 119-142.

545 Böhlke, J. K., & Irwin, J. J. *Earth Planet. Sc. Lett.* **1992**, 110(1), 51-66. DOI:10.1016/0012-
546 821X(92)90038-W

547 Boström, K., Frazer, J., Blankenburg, J., *Archiv Min. Geol* **1967,** 4, 477-485.

548 Brunauer, S.; Emmett, P. H.; Teller, E. *J. Am. Chem. Soc.* **1938**, 60 (2): 309–319. DOI:
549 10.1021/ja01269a023

550 Bosbach, D., Boettle, M., Metz, V. *SKB Technical Report.* **2010**, TR-10-43.

551 Brandt, F., Curti, E., Klinkenberg, M., Rozov, K., Bosbach, D. *Geochim. Cosmoch. Ac.* **2015**, 155, 1-
552 15. DOI:10.1016/j.gca.2015.01.016

553 Burkhard, A. *Schweiz. Miner. Petrog.* **1973**, 53, 185-197.

554 Ceccarello, S., Black, S., Read, D., Hodson, M. *Miner. Eng.* **2004**, 17, 323-330.
555 DOI:10.1016/j.mineng.2003.11.007

556 Curti, E., Fujiwara, K., Iijima, K., Tits, J., Cuesta, C., Kitamura, A., Müller, W. *Geochim. Cosmochim.*
557 *Acta* **2010**, 74 (12), 3553 3570. DOI:10.1016/j.gca.2010.03.018

558 Deer, W.A., Howie, R.A., Zussman, J., Introduction to the Rock-Forming Minerals. Third Edition.
559 Mineralogical Society, 2013.

560 De Yoreo J.J., Burnham A.K., Whitman P.K. *Int. Mater. Rev.* **2002**.47(3):113-52.

561 Doerner, H., Hoskins, W.M. *J. Am. Chem. Soc.* **1925**, 47, 662-675. DOI: 10.1021/ja01680a010

562 Frondel, C. *Am. Mineral.* **1935**, 20 (12), 853-862.

563 Gault, B., Moody, M.P., Cairney, J.M., Ringer, S.P., Atom Probe Microscopy. Springer Series in
564 Materials Science, 160, Springer, New York, Heidelberg, Dordrecht, London, 2012. DOI
565 10.1007/978-1-4614-3436-8
566 Geisler, T., Nagel, T., Kilburn, M.R., Janssen, A., Icenhower, J.P., Fonseca, R.O.C., Grange, M.,
567 Nemchin, A.A. *Geochim. Cosmochim. Acta* **2015**, 158 112-129. DOI:10.1016/j.gca.2015.02.039
568 Giannuzzi, L.A., Stevie, F.A. *Micron* **1999**, 30 (3), 197-204. DOI:10.1016/S0968-4328(99)00005-0
569 Gin, S., Ryan, J.V., Schreiber, D.K., Neeway, J., Cabié, M. *Chem. Geol.* **2013**, 349, 99-109.
570 DOI:10.1016/j.chemgeo.2013.04.001
571 Godinho, J.R.A., Stack. A.G., *Cryst. Growth Des.,* **2015**. 15 (5), 2064-2071. DOI: 10.1021/cg501507p
572 Gordon, L., Rowley, K. *Anal. Chem.* **1957**, 29, 34-37. DOI: 10.1021/ac60121a012
573 Gordon, L. M., Tran, L., Joester,D. *ACS nano* **2012**, 6 (12) 10667-10675. DOI: 10.1021/nn3049957
574 Grahmann, W. *Neues Jb. Miner. Abh.* **1920**
575 Grundl, T., Cape, M., *Ground water* **2006**, 44, 518-527. DOI: 10.1111/j.1745-6584.2006.00162.x
576 Hanor, J.S. *Rev. Mineral. Geochem.* **2000**, 40, 193-275.DOI: 10.2138/rmg.2000.40.4
577 Hellmann, R., Cotte,S., Cadel, E., Malladi, S., Karlsson, L.S., Lozano-Perez, S., Cabié, M., Seyeux, A.
578 *Nat. mat.* **2015**, 14(3), 307-311. DOI:10.1038/nmat4172
579 Horai, K. J. *Geophys. Res.* **1971**, 76 (5), 1278 1308. DOI: 10.1029/JB076i005p01278
580 Jaremalm, M. Köhler, M., Lidman, F. **2013**, SKB TR 13-28.
581 Judat, B., Kind, M. *Colloid Interf. Sci.* **2004**, 269, 341-353. DOI:10.1016/j.jcis.2003.07.047
582 Kelly, T.F., Larson, D.J. *Annu. Rev. Mater. Res.* **2012**, 42 (42), 1-31. DOI: 10.1146/annurev-matsci-
583 070511-155007
584 Klinkenberg, M., Brandt, F., Breuer, U., Bosbach, D. *Environ. Sci. Technol.* **2014**, 48, 6620-6627.
585 DOI: 10.1021/es405502e
586 Lendeking, C., Wheeler, H.A., *Am. Jour.* **1891**, 3, 42, 495.
587 Marques, B. *Cr. Acad. Sci. D. Nat.* **1934**. 198, 1765-1767.
588 Miller, M.K., Forbers, R.G., Atom-Probe Tomography: The Local Electrode Atom Probe. Springer,
589 New York, Heidelberg, Dordrecht, London, 2014. DOI 10.1007/978-1-4899-7430-3

590 Mayer, J., Giannuzzi, L.A., Kamino, T., Michael, *J. MRS Bull.* **2007**, 32, 400 – 407. DOI:
591 10.1557/mrs2007.63
592 Miller, M.K.; Russell, K.F.; Thompson, G.B. *Ultramicroscopy* **2005**, 102 (4), 287-298.
593 DOI:10.1016/j.ultramic.2004.10.011
594 Miller, M.K., Russell, K.F., Thompson, K., Alvis, R., Larson, D.J. *Microsc. Microanal.* **2007**, 13, 428-
595 436. DOI: 10.1017/S1431927607070845
596 Miller, M.K., Russel, K.F. *Ultramicroscopy.* **2007**, 107, 761-766. DOI:10.1016/j.ultramic.2007.02.023
597 Minster, T., Ilani, S., Kronfeld, J., Even, O., Godfrey-Smith, D. *J. Environ. Radioactivity* **2004**,71,
598 261-273.
599 Norrby, S. Andersson, J. Dverstorp, B. Kautsky, F., Lilja, C., Sjöblom, R., Sundström, B., Toverud, Ö.
600 **1997**, TR SKI Site 94.
601 Parr, D. F., & Chang, L. L. *Ohio J. Sci.* **1980**, V80, n1, 20-29.
602 Prieto, M., Putnis, A., Fernandez-Diaz, L. *Geol. Mag.* **1993,** 130, 289-289.
603 Prieto, M., Fernández-González, A., Putnis, A., Fernandez-Diaz, L. *Geochim. Cosmochim. Acta*
604 **1997**, 61(16), 3383-3397. DOI:10.1016/S0016-7037(97)00160-9
605 Putnis, A., Fernandez-Diaz, L., Prieto, M. *Nature*, **1992** *358*(6389), 743-745. DOI:10.1038/358743a0
606 Putnis, A. *Nat. mat.* **2015**, 14(3), 261-262. DOI:10.1038/nmat4198
607 Rajabzadeh, M.A. *J. .Sci. Technol.* **2007**, 31, A1.
608 Renock, D., Landis, J.D., Sharma, M., Appl. Geochem. 2016, 64, 73-86.
609 DOI:10.1016/j.apgeochem.2015.11.001
610 Rosenberg, Y.O., Metz, V., Oren, Y., Volkman, Y., Ganor, J. *Geochim. et Cosmochim. Acta* **2011**, 75,
611 5403-5422. DOI:10.1016/j.gca.2011.07.013
612 Ruiz-Agudo, C., Ruiz-Agudo, E., Putnis, C.V., Putnis, A. *Cryst. Growth Des.* **2015**, 15 (8), 3724-
613 3733.
614 Ruiz-Agudo, E., Putnis, C.V., Putnis, A. *Chem. Geol.* **2014**, 383, 132-146. DOI:
615 10.1021/acs.cgd.5b00315
616 Sabine, P., Young, B. *Acta Crystallograph.* **1954**, 7, 630.

617 Sachtleben, 2015. Safety Data Sheet according to Regulation (EC) No 1907/2006 to 1272/2008. Print
618 date: 09.06.2015; http://www.sachtleben.de/fileadmin/safety_data_sheets/blanc_fixe_xr_series_en.pdf
619 (Access date: 30.11.2015)
620 SKB 2011, Long-term safety for the final repository for spent nuclear fuel at Forsmark. TR-11-01
621 Takano, B., Watanuki, K., *Geochem. J.* **1974**, 8, 87-95.
622 Thompson, K., Lawrence, D., Larson, D.J., Olson, J.D., Kelly, T.F., Gorman, B. *Ultramicroscopy*,
623 **2007**, 107 (2-3), 131-139. DOI:10.1016/j.ultramic.2006.06.008
624 Vinograd, V. L., Brandt, F., Rozov, K., Klinkenberg, M., Refson, K., Winkler, B., Bosbach, D.
625 *Geochim. Cosmochim. Acta* **2013**, 122, 398 417. DOI:10.1016/j.gca.2013.08.028
626 Williams, D.B., Carter, C.B. Transmission Electron Microscopy. A Textbook for Materials Science.
627 2nd ed.; Springer, New York, 2009.
628 Wilkinson, J. J. *Lithos* **2001**, 55(1), 229-272. DOI:10.1016/S0024-4937(00)00047-5
629 Zaitseva N, Carman L. *Prog. Cryst. Growth Ch.* **2001**. 43(1):1-18.
630 Zhang, T., Gregory, K., Hammack, R. W., & Vidic, R. D. *Environ. Sci. Technol.* **2014**, 48(8)
631 4596-4603. DOI: 10.1021/es405168b
632 Zhang, T., Hammack, R.W., Vidic, R.D., *Environ. Sci. Technol.* **2015**, 49(15), 9347-9354. DOI:
633 10.1021/acs.est.5b01393
634 Zielinski, R., Otton, J., Budahn, J. *Environ. Poll.* **2001**, 113, 299-309.
635 Zielinski, R.A., Otton, J.K., 1999. Naturally Occurring Radioactive Materials (NORM) in Produced
636 Water and Oil-field Equipment: An Issue for Energy Industry. US Department of the Interior, US
637 Geological Survey.
638
639
640